Pressure-temperature phase diagram of lithium, predicted by embedded atom model potentials

Jordan Dorrell[†] and Livia B. Pártay[*,‡]

†*Department of Chemistry, University of Reading, Whiteknights, Reading, RG6 6AD, UK; moved to the School of Metallurgy and Materials, University of Birmigham, Edgbaston, Birmingham, B15 2TT, UK*

‡*Department of Chemistry, University of Reading, Whiteknights, Reading, RG6 6AD, UK; moved to the Department of Chemistry, University of Warwick, Gibbet Hill, Coventry, CV4 7EQ, UK*

E-mail: Livia.Bartok-Partay@warwick.ac.uk

Abstract

In order to study the performance of interatomic potentials and their reliability at higher pressures, the phase diagram of two different embedded-atom type potential models (EAM) and a modified embedded-atom model (MEAM) of lithium is compared. The calculations were performed by using the nested sampling technique in the pressure range $0.01 - 20$ GPa, in order to determine the liquid-vapour critical point, the melting curve and the different stable solid phases of the compared models. The low pressure stable structure below melting is found to be the body-centred-cubic (bcc) structure in all cases, but the higher pressure phases and the ground state structures show a great variation, being face-centred cubic (fcc), hexagonal close-packed (hcp), a range of different close packed stacking variants, and highly symmetric open structures are observed as well. A notable behaviour of the EAM model of Nichol and Ackland (PRB

2016) is observed, that the model displays a maximum temperature in the melting line, similarly to experimental results.

Introduction

Lithium, the third element of the periodic table, has been in the focus of research interest for many decades. It is widely used as one of the most important alloying compounds of aluminium and magnesium, it is a crucial component of batteries and electrodes, due to its large thermal conductivity and low viscosity, it is increasingly used as an effective coolant for nuclear reactors,[1,2] and it has also been proposed that liquid lithium could be implemented to shield plasma-facing components inside fusion reactors.[3,4]

In order to fully exploit the properties of Li both in engineering and in materials science applications, it is crucial to perceive its phase behaviour and the complex features of its phase diagram, several of which are not fully understood yet: the unusual trend of the melting line[5–10] which shows a maximum of 519 K at 10.3 GPa,[8] the lowest known melting point among elements at very high pressures (190 K around 50 GPa),[11] the predicted superconducting phase,[12–14] and the occurrence of exotic high pressure structures previously not seen in any other element, as suggested both by experimental observations[11] and *ab initio* random structure search calculations.[15,16]

Computational modelling techniques are now routinely used to augment experimental efforts in studying phase behaviour and predicting e.g. high-pressure materials properties, and providing an atomic level insight into physical processes. In the heart of these computations lies the potential model describing the atomic interactions. In order to compromise between accuracy and computational cost, in most large-scale and long-time simulations, empirical or semi-empirical descriptors are used. For lithium, similarly to most metals in the periodic table, several such interatomic potential models have been developed in the past decade within the Embedded Atom Method (EAM) framework. There are models developed

within the original EAM,[17–20] the modified EAM (MEAM)[21,22] which also includes an angular dependent term to make it more applicable for materials with directional bonding, and the 2NN-MEAM framework,[23–25] which also accounts for the interactions with the second nearest neighbour shell.

These potential models are usually determined by fitting a proposed functional form to a group of available data (e.g. bulk modulus, pair correlation functions or atomisation energy) which may be obtained from either experimental measurements or first-principles calculations. Although the models are then expected to reproduce these microscopic properties accurately, the calculated macroscopic properties, such as the melting transition or the relative stability of crystal polymorphs can vary widely, especially under conditions further away from the original fitting region, sometimes showing fundamental difference from experimentally observed behaviour. However, since the calculation of the phase diagram requires the laborious application of a range of different tools and techniques, our knowledge on how the different interatomic potential models behave macroscopically is often very limited. This lack of information on the phase diagram not only makes it difficult to choose which model is the most reliable to study certain processes, but can also seriously hinder our ability to interpret and trust computational predictions made by these models.

In the current work we show how the nested sampling technique can be used to overcome the computational bottleneck, and calculate the phase diagram of potential models in a straightforward way. We perform calculations using three different lithium EAM-type models and compare their resulting phase diagrams, discussing features including the critical point, the melting line and predicted solid phases.

Methods and models

Nested sampling calculations

Nested sampling (NS) is a Bayesian inference method,[26] that has been adapted to sample the potential energy landscape of atomistic systems,[27,28] calculate the quantum partition function,[29] and also to sample transition paths.[30]

Nested sampling is an iterative technique that comprehensively samples the potential energy surface (PES) through a series of nested enthalpy levels, starting from the high enthalpy region, representing the high-temperature gas phase and going towards the global minimum, which corresponds to the stable crystal structure at 0 K. The simulation is started by initialising a pool of K uniformly random configurations, usually referred to as walkers. At every iteration of the algorithm, the walker with the highest enthalpy (H_i) is recorded, with its corresponding phase space volume estimated as $[K/(K+1)]^i$.[26] This configuration is then removed from the set of K walkers and substituted by a new uniformly random configuration with the constraint that its enthalpy must be lower than the current H_i. As the phase space volume shrinks rapidly with decreasing enthalpy, randomly generating new configurations quickly becomes computationally impractical. Thus, instead, one of the existing walkers are randomly selected and cloned, and a random walk of L steps (changing the atomic coordinates, volume and shape of the simulation cell) is performed on the clone to generate a new sample. As the simulation progresses, lower enthalpy levels are explored until the global minimum (or a low enough enthalpy level) is reached. The partition function can be evaluated by substituting an arbitrary temperature, T, in

$$\Delta(N,p,T) \propto \sum_i \left[[K/(K+1)]^{i-1} - [K/(K+1)]^i \right] e^{-\frac{H_i}{k_B T}}, \tag{1}$$

where N is the number of particles, p is the pressure, and k_B is the Boltzmann constant. A detailed derivation of this equation can be found in Ref.[31]

The power of the method lies in its unique ability to enable the calculation of the partition function, and thus to derive thermodynamic properties from the sampling. NS has been shown to sample regions of the phase space around phase transitions most efficiently,[27] without any prior knowledge of the phases or minima structures. Moreover, since NS is a 'top-down' approach, it is not specific to a particular region of the phase diagram, and it is capable of screening phase transitions of a system in an automated way. Its usage in calculating the pressure-temperature phase diagram has been demonstrated for aluminium and the NiTi shape-memory alloy,[32] iron,[33] and different model systems.[31,34]

In the current work, nested sampling calculations were performed as described in Ref.,[31] using the pymatnest program package.[35] Each simulation was performed at a constant pressure with using 64 atoms in a simulation cell of variable shape and size. Initial configurations were generated randomly, and new samples were generated by performing Hamiltonian Monte Carlo (all-atom) moves,[31] and changing the volume and the shape of the cell by shear and stretch moves with a ratio of 1:2:2:2, respectively. The LAMMPS[36] package was used for the dynamics and evaluating the energy of configurations. The number of walkers and the length of the walk was chosen such that the position of the resulting heat capacity peak in independent parallel calculations differed by less than the half-width at full maximum of the peak. This meant that at lower pressures the number of walkers were typically around $1000 - 1200$, while above 10 GPa it was necessary to use $2600 - 3000$ walkers to sample the different basins accurately. We used $1200 - 2500$ random walk steps per iteration to generate new walker configurations.

Studied potential models for lithium

Six of the Li interatomic models known to us have been systematically compared by Vella et al.,[37] using molecular dynamics simulations to calculate the liquid density, surface tension and liquid-bcc transition temperature. Their work concluded, that the MEAM model proposed by Cui et al.,[23] which also includes second nearest neighbour interactions, show

an overall best agreement with experimental data. In the current work we provide comparison for further two models developed since their study, with placing more focus on phase transitions, including the solid region of the phase diagram, and in a much wider pressure range.

Nichol and Ackland[18] developed a series of EAM potentials to model alkali metals using minimum fitting parameters. They used the bcc lattice parameter, elastic constants, cohesive energy, unrelaxed vacancy formation energy, and fcc energy per atom above the bcc value, with the main aim to ensure comparability between group I metals. As a result, though the series of their potentials perform well, the largest discrepancy to experimental data is observed for lithium, with the melting temperature overestimated considerably. In case of Na and Li there is also a martensitic transition observed, to a complex close-packed structure at low temperature. We refer to their Li model as the Nichol-Ackland EAM in our work.

In 2017 Ko and Jeon published a potential model on the basis of the second nearest-neighbour modified EAM formalism. Instead of using specific microscopic properties for fitting the potential parameters, they utilised the force-matching algorithm by building a DFT database of atomic forces and energies for perfect and defected bcc, fcc and hcp structures both at 0 K and at finite temperature.[25] This model reproduces low pressure melting temperatures remarkably well, and also known to predict a martensitic phase transition to disordered polytype structures at very low temperatures. We refer to this model as the Ko-Jeon 2NN-MEAM throughout the paper.

Since we aim to investigate macroscopic properties at higher pressures as well, we decided to also include the EAM model of Belashchenko[20] in our study. This is a modification of a previous potential,[19] which originally used experimental density (both solid and liquid), elastic constants, vacancy formation energy and surface properties in fitting the model parameters, with high-pressure properties (thermal energy and thermal pressure of collective electrons) also taken into account in the modified version. It is expected that the model reproduces thermodynamic properties sufficiently up to 15-20 GPa.[20] However, the published

model is not smooth around the cutoff, and the energy value is positive at the proposed truncation distance of 7.5 Å. To overcome technical difficulties caused by this discontinuity, we extended the model by adding a spline which smoothly brings the potential functions to zero in a further 0.2 Å distance. Our tests show that this modification does not effect the liquid density, the low-pressure melting transition, nor the 0 K transition pressure between the bcc and fcc phases. This model is referred to as Belashchenko2013 EAM in this work.

Results

Liquid-vapour critical point

The liquid-vapour critical point of most metals are not accessible to conventional experimental study (exceptions are Hg, K, Cs and Rb),[38] due to the extreme high critical temperatures, though the knowledge of critical properties is important both from the theoretical and applications point of view. Thus, critical properties are usually estimated based upon empirical relationships between the critical temperature and other measured thermodynamic properties. In case of lithium, the range of estimated critical temperatures are $T_c = 3223$ K $\pm$ 600,[39] $T_c = 3474$ K[40] and $T_c = 3600$ K,[41] while the estimated critical pressure spans a wider range with values from $p_c = 0.069$ GPa $\pm$ 20%[39] to $p_c = 0.027$ GPa.[41]

To locate the critical point in the nested sampling calculations, we draw on the results of Bruce and Wilding:[42] for a finite system at and below the critical point, the density distribution appears as a bimodal distribution (at the temperature corresponding to the maximum of the heat capacity peak), while above the critical point, the density distribution transitions quickly to a unimodal distribution. We used this argument to estimate the critical pressure to be between the two adjacent sampling pressures where the modality of the distribution changes – we had demonstrated that results provided by this approach are in very good agreement with those calculated by the Gibbs ensemble Monte Carlo technique.[32] The corresponding critical density and temperature was determined as the point where the

gradient of the temperature-density curve is closest to zero. These curves are shown in Figure 1 for the low-pressure nested sampling runs, along with the estimated critical points for the different potential models. The calculated critical temperatures vary widely among the models, the Belashchenko2013 EAM overestimates it by about as much as the other two studied models underestimate it, and the calculated critical pressures are all on the lower end of range of the experimentally predicted values.

It is obvious from Fig. 1, that the density profile of the Belashchenko2013 EAM model is rather different from the other two potentials. Experimental liquid density[43] is compared to the density reproduced by the models in the inset of Fig. 1 for the temperature range 500-1300 K, and all three models perform reasonably well in this respect. The Ko-Jeon 2NN-MEAM consistently overestimates the density, but only by 2.7%, while the density-temperature line of the Nichol-Ackland EAM has a slightly different slope. The Belashchenko2013 EAM model shows an overall good agreement with experimental liquid densities, as was also shown by the comparative study of Vella et al.[37]

Table 1: Calculated and experimental values for critical temperature (T_c), critical pressure (p_c), critical density (ρ_c)

Property	Exp.[39]	Belashchenko 2013 EAM	Nichol--Ackland EAM	Ko-Jeon 2NN-MEAM
T_c / K	3223	4020	2330	2900
p_c / GPa	0.069	0.015	0.015	0.032
ρ_c / gcm^{-3}	0.1045	0.095	0.16	0.155

Melting and solid phases

We used primarily the peak positions of heat capacity curves to locate phase transitions. To aid the identification of the solid structures and help clarify the low temperature solid-solid phase transitions – in which case the peaks are often very small due to the small enthalpy difference between different crystalline structures – we also calculated the Steinhardt bond order parameters[44] and radial distribution functions. These enable us to identify and distinguish

different structures generated during the nested sampling calculation. This information can also be used to group the configurations and assign them to different basins of the PES. This allows us to calculate the contribution of each basin to the total partition function,[28] and thus determine which structure is most populated at a given temperature. The ground state structures were determined by minimising all candidate structures found by the sampling at a series of pressure values, and comparing the minimum enthalpy values.

We have to note, that since the calculations used 64 atoms, we can expect that the finite size effect is not negligible. Our previous systematic studies have shown that using 64 atoms causes the melting temperature to be overestimated, depending on the employed potential model, by approximately $6-10\%$,[32] thus, in the current case of lithium, our 64-atom nested sampling calculations will result a melting point $30-70$ K higher. Meanwhile, solid-solid transitions were found to have a significantly weaker dependence on the system size, if a difference could be observed at all. For clarity, we present the melting transition values in the paper as calculated with using 64 atoms, without any corrections, with error bars calculated from the full width at half maximum of the heat capacity peaks, which is a good indicator of the finite size effect. As the comparisons to published coexistence simulation results show, the melting temperature predicted by nested sampling differs by about the above expected amount.

In case of all three studied models we have identified different close-packed structures: the face centred cubic (fcc) and other polytype stacking sequences. We denote these with their shortest repeating sequence, where 'h' stands for the layer which is sandwiched by neighbouring layers being in the same stacking positions ('hexagonal', such as in the hcp crystal **A**B**A** sequence), and 'c' stands for the layer where its neighbours are in different stacking positions ('cubic', such as in the fcc crystal **A**B**C** sequence).

It has to be noted that experimental measurements had suggested a martensitic phase transition to such a close-packed polytype structure at very low temperatures.[45] The suggested 9R phase (which is equivalent to 'hhc' stacking in the above notation) has since

been questioned[46] and proven to be unstable,[47] with calculations showing that the direct transition between the fcc and 9R phase is forbidden.[48,49]

Belashchenko2013 EAM

The calculated pressure-temperature phase diagram of the Belashchenko2013 model is shown in Figure 2. The model shows the melting temperature to be increasing with pressure, overestimating the experimental melting point along the entire studied pressure range. At lower pressures, the body-centred-cubic (bcc) structure is the most stable phase, at all temperatures below the melting point. No other basins are explored by the sampling, suggesting that the thermodynamic contribution of other phases is negligible. Above 1.38 GPa the fcc phase becomes the ground state structure, and as the pressure is increased further, the bond order parameters suggest the appearance of a phase with fcc and hcp local environments mixed in equal ratio. Figure 3 illustrates this, showing the average Q_4 and W_4 order parameters of the configurations generated during the nested sampling calculation, at two different pressure values, demonstrating that multiple basins are sampled simultaneously. With inspecting configurations, this is identified as a 'hc' phase (sometimes also referred to as double hexagonal-close-packed), in all nested sampling calculations in the pressure range $10 - 15$ GPa. Calculating the partition function ratio of the competing phases reveals, that while the 'hc' phase is the global minimum, the contribution of the fcc phase is substantial, with the hcp phase appearing as well above 15 GPa, though it stays metastable under all conditions. Interestingly, as the pressure is increased further, the fcc becomes the most stable structure again.

Nichol-Ackland EAM

The Nichol-Ackland EAM is known to overestimate the melting point considerably,[18] compared to the other models studied here. The NS calculations agree with this, estimating the melting point to be 695 K at 0.1 GPa. However, while the predictions made in Ref[18]

by the Clausius-Clapeyron equation predicts a steadily increasing melting temperature with increasing pressure, the melting line calculated from the nested sampling results quickly diverge from this. We found the melting temperature to increase up to 2 GPa, where this trend turns, and the melting temperature starts to decreases, quite dramatically, until it reaches 450 K at 10 GPa, as it can be seen on the phase diagram, in Figure 6. As expected, in the range where the gradient of the melting line is negative, a decrease in density upon freezing can be observed: at 5 GPa the density decreases by less than 3% at the phase transition, while at 10 GPa the change is much more significant, 11%.

Above this pressure the melting point fluctuates between 400-450 K. To verify our nested sampling findings, we performed two-phase coexistence simulations using the LAMMPS package[36] with 2590 atoms at 15 GPa. These simulations resulted in the melting temperature to be estimated at 420 K.

Figure 4 shows the heat capacity curves for the Nichol-Ackland EAM model. As the pressure increases, not just the peak position, but the shape of the curve changes significantly too, to much sharper and taller.

Up to 5 GPa the Nichol-Ackland EAM model also predicts the bcc phase to be the most stable right below the melting point. However, at lower temperatures the picture becomes more complicated. As small peaks on the heat capacity curves indicate, there are solid-solid phase transition from the bcc phase, to a range of different ground-state structures according to the structural analysis. Below 0.3 GPa the low-temperature structure is a distorted bcc phase, where the cube formed by the eight nearest neighbours is elongated along the diagonal of one of the faces, forming a deltoid-based prism. In the periodic structure these prisms are arranged in an alternating orientation. This structure is denoted as bcc* on the phase diagram, and its characteristic neighbour distances are shown in Figure 5(a). As the pressure increases, another structure emerges as the ground state. This is very close to being close-packed, but at low temperature a very small but consistent neighbour distance difference becomes apparent, thus a layered structure, shown in Figure 5(b) as CP*, emerges.

These layers are formed by jagged sheets of atoms in rectangular arrangement, with the zig-zag motives being the alternative of polytype stackings in the close-packed structure. We performed both 64 and 60 atoms simulations to explore if a particular motive is more favourable than the others, but found that most stackings which can be accommodated in the cell are generated during the sampling.

Above 3.2 GPa these structures become properly close-packed, and as previously, NS finds a range of different stacking variants, all which has the same ground state enthalpies. At 5 GPa, fcc, hcp, hhcc and hc polytypes are all sampled with approximately equal probability within the same calculations, while at 10 GPa hhcc and hc stackings are found more frequently.

In the pressure range of $10.3 - 15.9$ GPa, an open structure emerges as the most stable phase, where atoms are layered in jagged sheets of rectangular arrangement. These sheets are shifted with respect to each other, with every second layer being in the same lateral position, as shown in Figure 5(c). This structure has Cmcm symmetry with four atoms in the unit cell, and has a 22% higher density than the close packed phase.

As the pressures increases above 15.9 GPa, the zigzag sheets flatten out and become parallel, with atoms being in a perfect square arrangement within each layer. This structure has I4/mmm symmetry, a body-centred-tetragonal structure, having a further 21% increase in the density. The structure is shown in Figure 5(d) along characteristic atom-atom distances.

To test whether these structures can potentially be stable experimentally, they were all minimised using density-functional theory at pressures 0, 5 and 20 GPa. DFT calculations were performed with the CASTEP package,[51,52] with the PBE functional using a cutoff energy of 700 eV[53] and a k-point spacing[54] of 0.015 $Å^{-1}$. The I4/mmm structure was transformed to fcc, while the CP* structures all minimised into the corresponding close packed stacking variants. The Cmcm structure was found to be stable, but having significantly higher energy than the fcc configuration. Though these exotic phases did not prove to be relevant in the experimental phase diagram, nor identical to the unique solid structures

lithium is known to stabilise in (cI16 and oC88)[11] at high pressures, it is remarkable that the Nichol-Ackland EAM model forms a variety of stacking variants at low pressure, and non close-packed crystals upon the drop in the melting temperature, a feature not seen in the other models, but observed experimentally.

Ko-Jeon 2NN-MEAM

The Ko-Jeon 2NN-MEAM model is known to reproduce the low pressure melting line very accurately,[25] and the NS results are also aligned with this. Below the melting transition an additional peak appears on the heat capacity curves, suggesting the presence of a solid-solid phase transition at lower temperatures. Calculating the bond order parameters reveals, that the bcc phase formed upon freezing transforms to fcc at around 100 K. Though the corresponding heat capacity peak almost diminishes as the pressure increases, the bcc-fcc transition remains obvious, moreover, above 8 GPa, an additional phase can be clearly distinguished from the Q_4 and W_4 order parameter plots: a phase with 1:1 ratio of fcc and hcp neighbourhoods, as seen in case of the 10 GPa simulation in Figure 7. Inspecting configurations show that this is exclusively realised as the hhcc phase, i.e. two layers of hcp and two layers of fcc alternating.

In order to check that the 64 atom cell does not restrict our calculations to only a certain group of polytypes, a simulation with 60 atoms was performed at 12 GPa. This resulted in phase transitions at the same temperatures as the 64-atom calculations, and although a small number of other stacking variants (hc and hcchc) were generated, the large majority of the structures still had the hhcc stacking arrangement between 100-200 K.

Conclusions

We have used the nested sampling technique to calculate the pressure-temperature phase diagram of three interatomic potential models of lithium, and compare their behaviour.

In the three models different microscopic properties were taken into account, and different procedures were used in fitting the functional forms of the potential. Low pressure-low temperature bcc and fcc structures were included in some form in all three of them, thus the ground state structure and potentially the transitions between low pressure solid phases can be expected to be close to experimental findings. Indeed, our calculations found that all models crystallise into the bcc structure upon freezing, at least at the lower pressure range, but the ground state structure varied between being bcc, fcc or a complex distorted stacking variant of these. While the Nichol-Ackland and the Belashchenko2013 models both have at least a bcc–close-packed transition with a phase boundary comparable to experimental results, the Ko-Jeon 2NN-MEAM shows even less resemblance to the experimental phase diagram, which is surprising given that an extensive database of DFT forces and energies were included during the fitting, also at finite temperature.

The high-pressure behaviour of the models varied even more widely. We observed different close-packed stacking phases in all cases, and for the Nichol-Ackland model several additional highly symmetric open structures were found to be stable too. Even though these structures are not necessarily relevant in terms of the experimental phase diagram of lithium, it strongly demonstrates that the macroscopic properties of interatomic potential models can be very different from what is expected; the discovered open structures would have been very unlikely to be considered as candidate structures in e.g. classic free energy or coexistence calculations. Overall, our results suggest that none of the models can be used reliably to study high pressure properties of lithium.

The low-pressure melting point predicted by the nested sampling agrees well with the available literature values for the different models, but it is also clear that simply extrapolating values at higher pressures can be misleading. The discovered negative gradient of the melting-line in case of the Nichol-Ackland EAM demonstrates this. The melting lines show good agreement with experimental results for the Belashchenko2013 and Ko-Jeon models, with the largest discrepancy seen in case of the Nichol-Ackland EAM, the only one not in-

cluding finite temperature properties in the potential fitting. However, this model shows the unusual feature of the lithium properties, a maximum in the melting line.

Our comparisons showed that the studied models all underestimate the critical pressure, but given that none of the models include any gas-phase, single-atom or cluster properties during fitting, it is remarkable that they all predict critical properties in the right order of magnitude.

We can conclude that the way the fitting parameters affect the macroscopic behavior is complex, simply considering the choice of microscopic properties does not provide the full picture. These findings not only emphasise the importance of unbiased sampling methods in mapping out the phase diagram of interatomic potential models, but also illustrate that our general understanding of their macroscopic behaviour needs to be improved and further systematic investigations are necessary.

Acknowledgement

Via the authors' membership of the UK's HEC Materials Chemistry Consortium, which is funded by EPSRC (EP/L000202), this work used the ARCHER UK National Supercomputing Service (http:// www.archer.ac.uk). LBP acknowledges support from the EPSRC through an Early Career Fellowship (EP/T000163/1).

Data Availability

Simulation data and configurations are made openly available from the University of Warwick Research Portal at http://wrap.warwick.ac.uk/136306/.

References

(1) Ivanovsk, M. N.; Morozov, M. N.; Loginov, N. I. *Lithium as a coolant in nuclear power installations*; 2005; International Atomic Energy Agency, 11. meeting of the International Association for Hydraulic Research (IAHR) working group, reference: 37032246.

(2) Holroyd, R. J.; Mitchell, J. T. D. Liquid lithium as a coolant for Tokamak fusion reactors. *Nucl. Eng. Des./Fusion* **1983**, *1*, 17–38.

(3) Moir, R. Liquid first walls for magnetic fusion energy configurations. *Nucl. Fusion* **1997**, *37*, 557–566.

(4) Ou, W.; Zheng, X. J.; Gou, F. J.; Deng, B. Q.; Peng, L. L.; Cao, X.; Zhang, W. W.; Xue, X. Y. A physical model of an ejection suppressed CPS liquid lithium divertor target. *Nucl. Fusion* **2015**, *55*, 043015–040326.

(5) Newton, R. C.; Jayaraman, A.; Kennedy, G. C. The fusion curves of the alkali metals up to 50 kilobars. *J. Geophys. Res.* **1962**, *67*, 2559–2569.

(6) Schaeffer, A. M. J.; Talmadge, W. B.; Temple, S. R.; Deemyad, S. High pressure melting of lithium. *Phys. Rev. Lett.* **2012**, *109*, 185702.

(7) Luedemann, H. D.; Kennedy, G. C. Melting curves of lithium, sodium, potassium, and rubidium to 80 kilobars. *J. Geophys. Res.* **1968**, *73*, 2795–2805.

(8) Lazicki, A.; Fei, Y.; Helmey, R. J. High-pressure differential thermal analysis measurements of the melting curve of lithium. *Solid. State. Commun.* **2010**, *150*, 625–627.

(9) Tamblyn, I.; Raty, J.-Y.; Bonev, S. A. Tetrahedral clustering in molten lithium under pressure. *Phys. Rev. Lett.* **2008**, *101*, 075703.

(10) Kechin, V. V. Melting curve equations at high pressure. *Phys. Rev. B.* **2001**, *65*, 052102.

(11) Guillaume, C. L.; Gregoryanz, E.; Degtyareva, O.; McMahon, M. I.; Hanfland, M.; Evans, S.; Guthrie, M.; Sinogeikin, S. V.; Mao, H.-K. Cold melting and solid structures of dense lithium. *Nature* **2011**, *7*, 211–214.

(12) Tuoriniemi, J.; Juntunen-Nurmilaukas, K.; Uusvuori, J.; Pentti, E.; Salmela, A.; Sebedash, A. Superconductivity in lithium below 0.4 mK at ambient pressure. *Nature* **2007**, *447*, 187–189.

(13) Struzhkin, V. V.; Eremets, M. I.; Gan, W.; kwang Mao, H.; Hemley, R. J. Superconductivity in dense lithium. *Science* **2002**, *298*, 1213–1215.

(14) Deemyad, S.; Schilling, J. S. Superconducting phase diagram of Li metal in nearly hydrostatic pressures up to 67 GPa. *Phys. Rev. Lett.* **2003**, *91*, 167001.

(15) Pickard, C. J.; Needs, R. J. Dense low-coordination phases of lithium. *Phys. Rev. Lett.* **2009**, *102*, 146401.

(16) Tsuppayakorn-aek, P.; Luo, W.; Watcharatharapong, T.; Ahuja, R.; Bovornratanaraks, T. Structural prediction of host-guest structure in lithium at high pressure. *Sci. Rep.* **2018**, *8*, 5278.

(17) Belashchenko, D. K.; Ostrovskii, O. I. Application of the embedded atom model to liquid metals: liquid lithium. *High Temp.* **2009**, *47*, 231–237.

(18) Nichol, A.; Ackland, G. J. Property trends in simple metals: An empirical potential approach. *Phys. Rev. B* **2016**, *93*, 184101.

(19) Belashchenko, D. K. Electron contribution to energy of alkali metals in the scheme of an embedded atom model. *High Temp.* **2012**, *50*, 331–339.

(20) Belashchenko, D. K. Impact compression of alkali metals: Computer-aided simulation. *High Temp.* **2013**, *51*, 626–639.

(21) Baskes, M. I. Modified embedded-atom potentials for cubic impurities. *Phys. Rev. B* **1992**, *46*, 2727–2742.

(22) Yuan, X.; Takahashi, K.; Yin, Y.; Onzawa, T. Development of modified embedded atom method for a bcc metal: lithium. *Model. Simul. Mater. Sci. Eng.* **2003**, *11*, 447–456.

(23) Cui, Z.; Gao, F.; Cui, Z.; QU, J. Developing a second nearest-neighbor modified embedded atom method interatomic potential for lithium. *Modelling Simul. Mater. Sci. Eng.* **2012**, *20*, 1–12.

(24) Kim, Y.-M.; Jung, I.-H.; Lee, B.-J. Atomistic Modeling of Pure Li and Mg-Li System. *Modelling Simul. Mater. Sci. Eng.* **2012**, *20*, 035005.

(25) Ko, W.-S.; Jeon, J. B. Interatomic potential that describes martensitic phase transformations in pure lithium. *Comput. Mater. Sci.* **2017**, *129*, 202–210.

(26) Skilling, J. Nested sampling for general Bayesian computation. *Bayesian Anal.* **2006**, *735*, 833–859.

(27) Pártay, L. B.; Bartók, A. P.; Csányi, G. Efficient sampling of atomic configurational spaces. *J. Phys. Chem B* **2010**, *114*, 10502–10512.

(28) Dorrell, J.; B. Pártay, L. Thermodynamics and the potential energy landscape: case study of small water clusters. *Phys. Chem. Chem. Phys.* **2019**, *21*, 7305–7312.

(29) Szekeres, B.; Pártay, L. B.; Mátyus, E. Direct computation of the quantum partition function by path-integral nested sampling. *J. Chem. Theory Comput.* **2018**, *14*, 4353–4359.

(30) Bolhuis, P. G.; Csányi, G. Nested transition path sampling. *Phys. Rev. Lett.* **2018**, *120*, 250601.

(31) Baldock, R. J. N.; Bernstein, N.; Salerno, K. M.; Pártay, L. B.; Csányi, G. Constant-pressure nested sampling with atomistic dynamics. *Phys. Rev. E* **2017**, *96*, 43311–43324.

(32) Baldock, R. J. N.; Pártay, L. B.; Bartók, A. P.; Payne, M. C.; Csányi, G. Determining pressure-temperature phase diagrams of materials. *Phys. Rev. B* **2016**, *93*, 174108.

(33) Pártay, L. B. On the performance of interatomic potential models of iron: Comparison of the phase diagrams. *Comput. Mater. Sci* **2018**, *149*, 153–157.

(34) Pártay, L. B.; Bartók, A. P.; Csányi, G. Nested sampling for materials: The case of hard spheres. *Phys. Rev. E* **2014**, *89*, 022302.

(35) Bernstein, N.; Baldock, R. J. N.; Pártay, L. B.; Kermode, J. R.; Daff, T. D.; Bartók, A. P.; Csányi, G. pymatnest. `https://github.com/libAtoms/pymatnest`, 2016.

(36) Plimpton, S. Fast parallel algorithms for short-range molecular dynamics. *J. Comp. Phys.* **1995**, *117*, 1–19.

(37) Vella, J. R.; Stillinger, F. H.; Panagiotopoulos, A. Z.; Debenedetti, P. G. A comparison of the predictive capabilities of the embedded-atom method and modified embedded-atom method potentials for lithium. *J. Phys. Chem. B* **2015**, *119*, 8960–8968.

(38) Hensel, F.; Marceca, E.; Pilgrim, W. C. The metal–non-metal transition in compressed metal vapours. *J. Phys.: Condens. Matter* **1998**, *10*, 11395–11404.

(39) Dillon, I. G.; Nelson, P. A.; Swanson, B. S. Measurement of densities and estimation of critical properties of the alkali metals. *J. Chem. Phys.* **1966**, *44*, 4229–4238.

(40) Azad, A. M.; Ganesan, S.; Sreedharan, O. Internal pressure approach for the estimation of critical temperatures of Li(l), K(l) and NaK(l). *J. Nucl. Mat.* **1984**, *126*, 83–85.

(41) Nikolaev, D. N.; Ternovoi, V. Y.; Pyalling, A. A.; Kvitov, S. V.; Fortov, V. Investigation on near critical point states of lithium, sodium and aluminium by pulse heating during launching. *AIP Conf. Proc.* **2009**, *1195*, 923–926.

(42) Bruce, A. D.; Wilding, N. B. Scaling fields and universality of the liquid-gas critical point. *Phys. Rev. Lett.* **1992**, *68*, 193.

(43) Yakimovich, K. A.; Mozgovoi, A. G. Experimental investigation of the density and surface tension of molten lithium at temperatures up to 1300 K. *High Temp.* **2000**, *4*, 657–659.

(44) Steinhardt, P. J.; Nelson, D. R.; Ronchetti, M. Bond-orientational order in liquids and glasses. *Phys. Rev. B* **1983**, *28*, 784.

(45) Vaks, V. G.; Katsnelson, M. I.; Koreshkov, V. G.; Likhtenstein, A. I.; Parfenov, E.; Skok, V. F.; Sukhoparov, V. A.; Trefilov, A. V.; Chernyshov, A. A. An experimental and theoretical study of martensitic phase transitions in Li and Na under pressure. *J. Phys.: Condens. Matter* **1989**, *1*, 5319–5335.

(46) Elatresh, S. F.; Cai, W.; Ashcroft, N. W.; Hoffmann, R.; Deemyad, S.; Bonev, S. A. Evidence from Fermi surface analysis for the low-temperature structure of lithium. *Proc. Natl. Acad. Sci. U. S. A.* **2017**, *114*, 5389–5394.

(47) Ackland, G. J.; Dunuwille, M.; Martinez-Canales, M.; Loa, I.; Zhang, R.; Sinogeikin, S.; Cai, W.; Deemyad, S. Quantum and isotope effects in lithium metal. *Science* **2017**, *356*, 1254.

(48) Loach, C. H.; Ackland, G. J. Stacking Characteristics of Close Packed Materials. *Phys. Rev. Lett.* **2017**, *119*, 205701.

(49) Pártay, L. B.; Ortner, C.; Bartók, A. P.; Pickard, C. J.; Csányi, G. Polytypism in the

ground state structure of the Lennard-Jonesium. *Phys. Chem. Chem. Phys.* **2017**, *19*, 19369–19376.

(50) Hanfland, M.; Syassen, K.; Christensen, N. E.; Novikov, D. L. New high-pressure phases of lithium. *Nature* **2000**, *408*, 174–178.

(51) Clark, S. J.; Segall, M. D.; Pickard, C. J.; Hasnip, P. J.; Probert, M. J.; Refson, K.; Payne, M. First principles methods using CASTEP. *Z. Kristall.* **2005**, *220*, 567–570.

(52) Payne, M. C.; Teter, M. P.; Allan, D. C.; Arias, T.; Joannopoulos, J. D. Iterative minimization techniques for ab initio total-energy calculations - molecular-dynamics and conjugate gradients. *Rev. Mod. Phys.* **1992**, *64*, 1045–1097.

(53) Francis, G. P.; Payne, M. C. Finite basis set corrections to total energy pseudopotential calculations. *J. Phys.-Condes. Matter* **1990**, *2*, 4395–4404.

(54) Monkhorst, H. J.; Pack, J. D. Special points for Brillouin-zone integrations. *Phys. Rev. B* **1976**, *13*, 5188–5192.

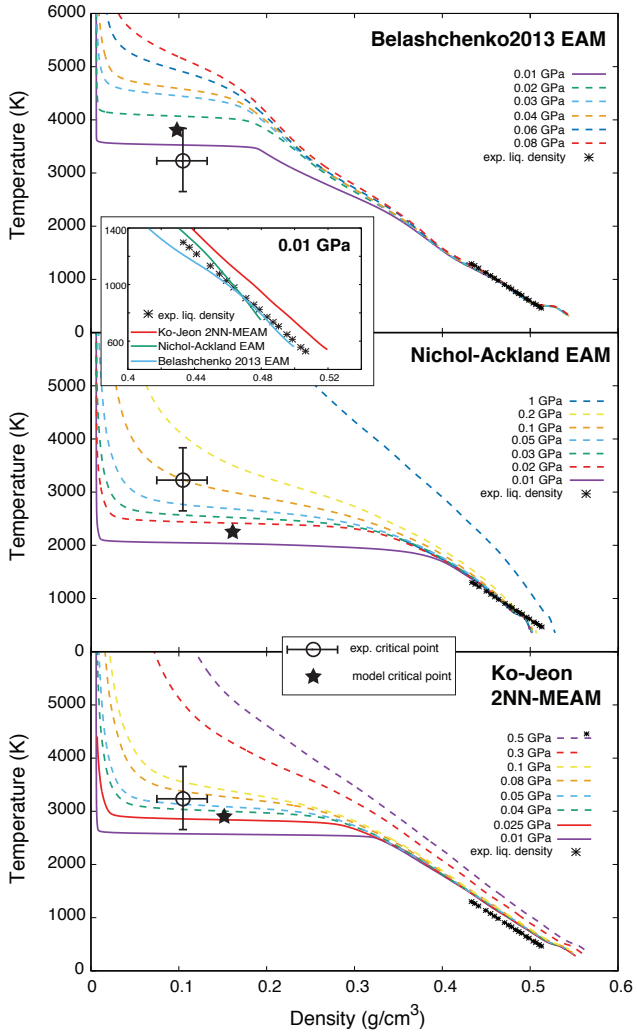

Figure 1: Estimate of critical point for the studied models. Black star represent the critical point estimated from nested sampling, density-temperature curves below and above the critical pressure are shown by solid and dashed lines, respectively. Open circle shows experimentally predicted critical values,[39] black crosses show experimental liquid densities.[43]

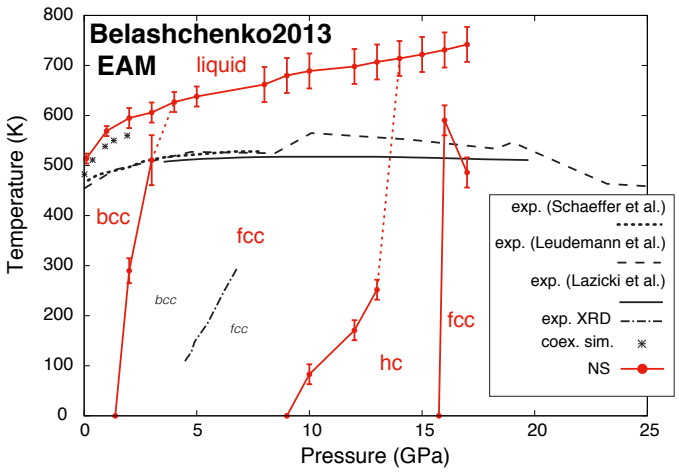

Figure 2: Phase diagram of the Belashchenko2013 EAM model. Experimental melting lines and the bcc-fcc phase boundary, shown by black lines, are from.[6–8,11,50] Black asterisks are melting points determined by 2-phase coexistence simulations, from Ref.[37]

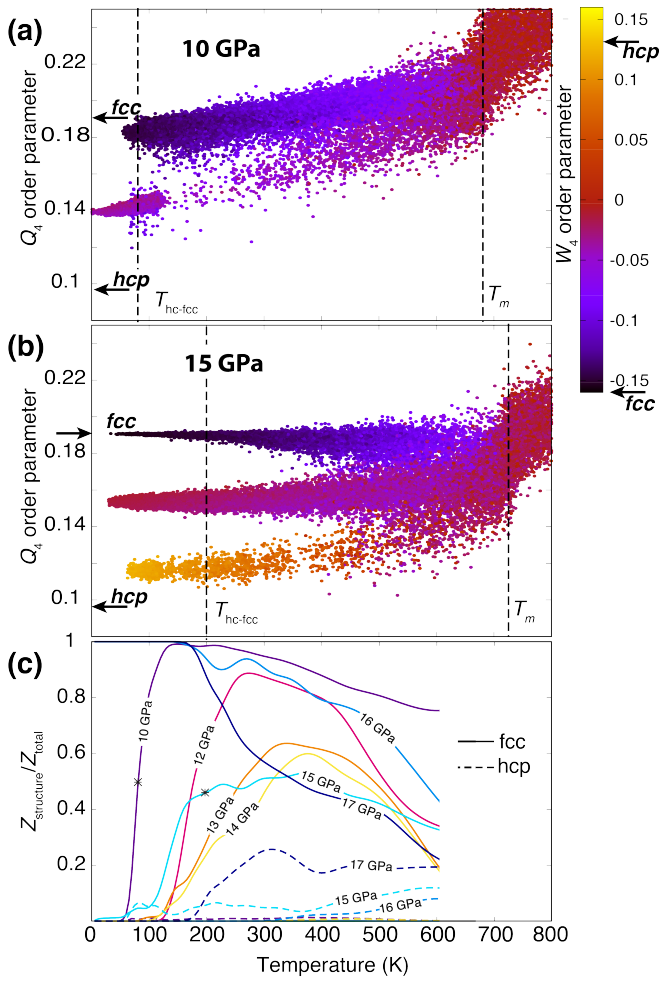

Figure 3: Basins explored with the Belashchenko2013 EAM model during the nested sampling. Upper two panels show the average Q_4 bond order parameter as a function of temperature of configurations generated during nested sampling at (a) 10 GPa and (b) 15 GPa. Each dot corresponds to a single configuration and is coloured according to the average W_4 bond order parameter. Typical order parameter values for the hcp and fcc structures are shown by black arrows. Phase transition temperatures are shown by vertical dotted lines. (c) Partition function ratio of the fcc (solid lines) and hcp (dashed lines) structures at different pressure values. Asterisks indicate the phase transition points also shown in panel (a) and (b).

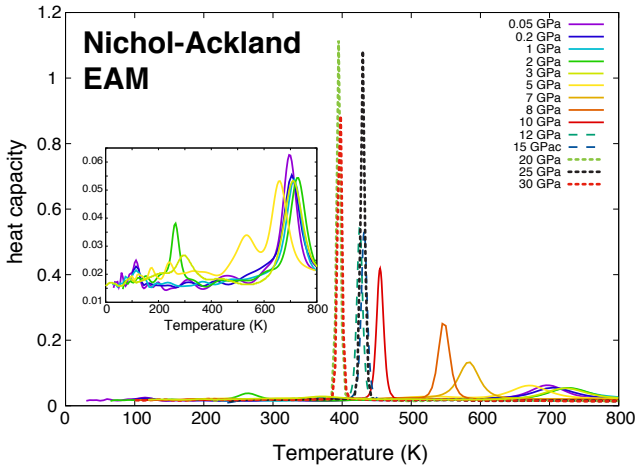

Figure 4: Heat capacity curves at different pressures calculated for the Nichol-Ackland potential. The inset shows data for the lower pressure runs on a different scale.

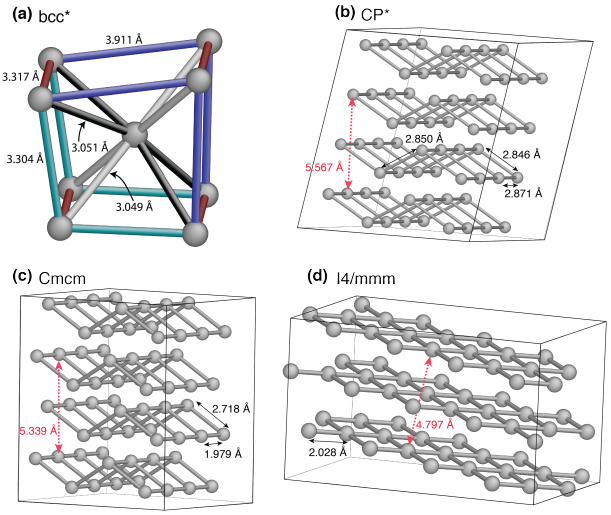

Figure 5: Non-close packed solid structures found by nested sampling calculations performed with the Nichol-Ackland EAM model. (a) Distorted bcc structure: bonds with the same colour have the same length (b) CP* structure (seen above 0.3 GPa) (c) Cmcm (seen above 10.3 GPa)and (d) I4/mmm (seen above 15.9 GPa) phases found by nested sampling . Neighbour distances and distance between layers of the same stacking positions are shown by black and red labels, respectively.

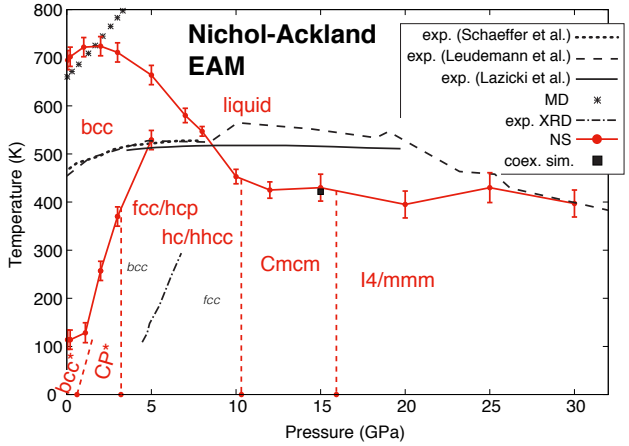

Figure 6: Phase diagram of the Nichol-Ackland EAM model. Experimental melting lines and the bcc-fcc phase boundary, shown by black lines, are from,[6–8,11,50] melting temperatures were calculated from a single MD simulation and using the Clausius-Clapeyron equation.[18]

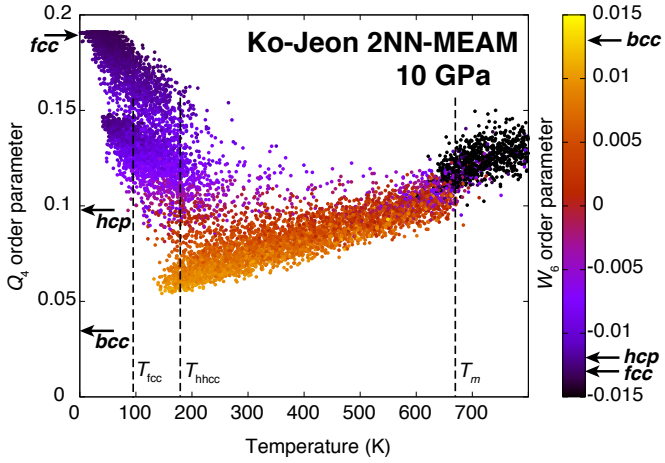

Figure 7: Q_4 bond order parameter of the configurations as a function of temperature, coloured by the W_6 order parameter. The points represent the configurations generated during a nested sampling run with the Ko-Jeon 2NN-MEAM potential at 10 GPa. The dashed lines mark the phase transition temperatures, and order parameters of the perfect crystal structures are labelled and marked by arrows.

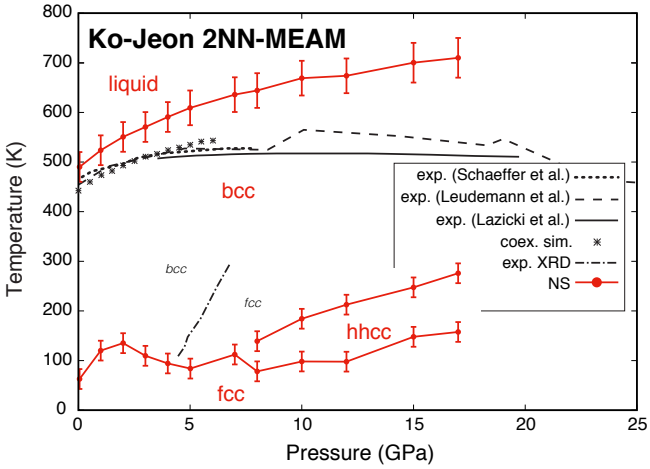

Figure 8: Phase diagram of the Ko-Jeon 2NN-MEAM model. Experimental melting lines and the bcc-fcc phase boundary, shown by black lines, are from,[6–8,11,50] melting temperatures calculated by MD simulations are shown by asterisks.[25]